ACS APPLIED MATERIALS & INTERFACES

Research Article

www.acsami.org

Exploration of Zn Resonance Levels and Thermoelectric Properties in I-Doped PbTe with ZnTe Nanostructures

P. K. Rawat,[†] B. Paul,[‡] and P. Banerji*,[†]

[†]Materials Science Centre, Indian Institute of Technology, Kharagpur 721302, India

[‡]Energy Materials Group, Thin Film Physics Division, Department of Physics, Chemistry, and Biology (IFM), Linköping University, Linköping 58183, Sweden

Supporting Information

ABSTRACT: Motivated by the theoretically predicted Zn resonant states in the conduction band of PbTe, in the present work, we investigated the effect of Zn substitution on the thermoelectric properties in I-doped n-type PbTe. The room temperature thermopower values show good agreement with the theoretical Pisarenko plot of PbTe up to a carrier concentration of 4.17×10^{19} cm^{-3}; thus, the presence of Zn resonance levels is not observed. Because of the low solubility of Zn in PbTe, a second phase of coherent ZnTe nanostructures is observed within the PbTe host matrix, which is found to reduce the lattice thermal conductivity. The reduced lattice thermal conductivity in PbTe by ZnTe nanostructures leads to notable enhancement in the figure of merit with a maximum value of 1.35 at 650 K. In contrast to the recent literature, the carrier mobility is not found to be affected by the band offset between ZnTe nanostructures and PbTe. This is explained by the quantum tunneling of the charge carrier through the narrow offset barrier and depletion width and coherent nature of the interface boundary between the two phases, i.e., ZnTe and PbTe.

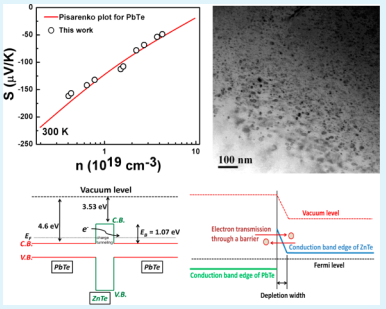

KEYWORDS: *resonant states, coherent nanostructures, lattice thermal conductivity, band offset, thermoelectric figure of merit*

INTRODUCTION

In the past few decades, thermoelectric materials have made a great impact on energy research because of their efficient ability in the conversion of heat into electricity for environmentally friendly power generation applications.[1−4] For an effective energy conversion, a thermoelectric material should exhibit high values of dimensionless thermoelectric figure of merit (zT), expressed as $[S^2\sigma/(\kappa_l + \kappa_e)]T$, where S is the thermopower, σ is the electrical conductivity, T is the absolute temperature, and κ_l and κ_e are the lattice and electronic thermal conductivities, respectively.[5,6] For a high value of zT, the numerator part ($S^2\sigma$), known as the power factor, should be enhanced with simultaneous reduction in the denominator, i.e., the total thermal conductivity $\kappa = \kappa_l + \kappa_e$. However, except κ_l, which is relatively independent from the other interdependent parameters, optimization of one parameter progressively deteriorates the other parameters.[7] Because, unlike other parameters (which depend mainly on electron transport), κ_l is determined only by phonon transport, intensive attention has been given to minimize this parameter through nanostructuring and atomic mass fluctuations in the material system.[8−19] In general, it has been observed that nanostructuring deteriorates the carrier mobility (thus the electrical conductivity) by interface-boundary scattering and band offset between the different phases.[20] However, endotaxial nanostructures without any band offset with the host matrix do not show such unwanted effects in mobility.[14,15] The interdependent parameters have also been decoupled quasi-independently by some successful strategies such as modulation doping,[21,22] energy barrier filtering,[8,23] optimization of the carrier concentration,[24−26] heavy-hole-dominated conduction,[27] and distortion in the density-of-states by resonant impurities[28−30] for an enhanced thermoelectric performance in the material system. Recent studies on Yb-doped $PbTe_{1-x}I_x$ clearly showed the interdependency of various thermoelectric parameters by impurity band-induced transport.[31] Heremans et al.[28] reported double-degree enhancement of the thermoelectric efficiency in PbTe by the incorporation of Tl resonant states. Zhang et al.[29] reported a zT value of 1.3 at 850 K in n-type PbSe by Al resonant states. Jaworski et al.[30] showed that Sn modifies the density-of-states of Bi_2Te_3 by about 15 meV below the valence band edge, leading to strong enhancement in its thermoelectric power. However, because of Fermi level pinning, all resonant impurities are not favorable to thermoelectric power enhancement. Ti is found to create its resonant states at approximately 52 meV inside the conduction band of PbTe; however, because of localization of the charge carriers due to Fermi level pinning, it does not contribute to the conduction process and thus to the thermopower.[32] Jovovic et al.[33] also reported a similar effect of Fermi level pinning on thermoelectric transport in In-doped $Pb_{1-x}Sn_xTe$. The theoretical calculations of Ahmad et al.[34] show that the divalent group IIB s-type impurities (Zn, Cd, and Hg) introduce resonant states near the bottom of the PbTe conduction band. An experimental attempt by Ahn et al.[35] on

Received: November 27, 2013
Accepted: February 27, 2014
Published: February 27, 2014

the thermoelectric properties of a PbTe−CdTe system does not show any enhancement in the thermopower. The reason could be the position of such levels inside the conduction band, i.e., very deep inside the band and due to which the required carrier concentration could not be achieved to place the Fermi level at the modified density-of-states, as was found for the Al resonant states in PbTe.[36]

Motivated to experimentally explore the predicted Zn resonant states and their effect on the thermoelectrical properties in PbTe, in the present work, we investigated I-doped PbTe:ZnTe because such kinds of investigations have not been reported in such a material system. With Zn being isovalent with Pb, it could not contribute to the carrier concentration. PbI_2 is introduced as an n-type dopant to tune the carrier concentration and Fermi level in the conduction band of PbTe.

EXPERIMENTAL SECTION

Synthesis. For the synthesis of samples of PbI_2-doped PbTe:ZnTe, the constituent elements, viz., 5 N pure elemental Pb (Alfa Aesar), Te (Sigma Aldrich), and Zn (Alfa Aesar) and 5 N pure PbI_2 (Sigma Aldrich), were taken in an appropriate stoichiometric ratio in a C-coated fused-silica ampule and sealed under high vacuum (~10^{-5} Torr). Then the sealed ampules were placed in a vertical furnace at 1273 K for 6 h. The obtained poor-quality ingots were hand-ground into powder by mortar and pestle. The ground powder was again filled in C-coated fused-silica ampules and vacuum-sealed. The powder-filled ampules were heated with oxyacetylene torch flames until the powder was completely melted and then air-cooled for consolidation. Dense polycrystalline (isotropic) and homogeneous (discussed in the Supporting Information, section SI-1) cylindrical ingots of typical length ~1.5 cm with silver metallic shine were obtained by the process. The obtained ingots were sliced into circular disks of diameter 10.2 mm, mechanically lapped with a 5 μm silicon carbide powder, and mirror-polished with alumina (Al_2O_3) abrasive for electrical measurements (Hall and resistivity). Then the disk-shaped samples were cut diagonally into bar form of dimensions 1.5 × 1.5 × 10 mm^3 for themopower measurements. The nomenclature of all of the samples and their corresponding mol % of ZnTe and PbI_2 along with their elemental compositions are presented in Table 1.

X-ray Diffraction (XRD). Powder XRD patterns were collected using Co Kα radiation (λ = 1.7902 Å) under reflection geometry on a PANalytical diffractometer operated at 40 kV and 30 mA.

Electrical Properties. The temperature-dependent electrical resistivity ($\rho = 1/\sigma$) and Hall coefficient (R_H) measurements were conducted under a van der Pauw configuration[37] using a locally made probe apparatus. A magnetic field value of ±1 T was employed for Hall measurements. Thermopower measurements were performed using a home-built apparatus described elsewhere.[38] For the measurement, bar-shaped samples were mounted between two Cu heating blocks using a spring assembly. To nullify the effect of superfluous electromotive force in thermopower measurements, a differential steady-state method was employed.[38,39] The temperature difference between the Cu blocks was examined by using K-type chromel−alumel thermocouples. All of the above measurements were done under dynamic vacuum conditions. Resistivity, Hall, and thermopower measurements were done during both heating and cooling cycles. The experimental uncertainties in the resistivity, Hall, and thermopower measurements were found to be 2, 3, and 5%, respectively.

Thermal Measurements. The temperature-dependent thermal diffusivity (D) was directly measured by a laser flash method under ambient nitrogen using a NETZSCH LFA 427 instrument. The specific heat (C_p) was derived by differential scanning calorimetry using a NETZSCH DSC 200-F3 instrument. The thermal conductivity was calculated as $\kappa = C_pD\delta$, where δ stands for the density of the sample, determined by the Archimedes method. After several cycles of experiments, the uncertainty in the thermal conductivity measurements was found to be 3%.

Transmission Electron Microscopy (TEM). Samples for TEM investigations were prepared by conventional methods of lapping, ultrasonic disk cutting, dimple grinding, and ion milling. High-resolution TEM (HRTEM) images and selected-area electron diffraction (SAED) patterns were obtained at 200 keV using a JEOL JEM 2100 microscope.

Table 1. Nomenclature of All of the Samples and Their Corresponding mol % of ZnTe and PbI_2 along with their Elemental Compositions

			elemental content (g)			
sample	ZnTe content (mol %)	PbI_2 content (mol %)	Pb	Te	Zn	PbI_2
S1	1	0.015	3	1.866	0.0095	0.001
S2	1	0.025	3	1.866	0.0095	0.0017
S3	1	0.050	3	1.866	0.0095	0.0033
S4	1	0.075	3	1.866	0.0095	0.005
S5	1	0.150	3	1.866	0.0095	0.01
S6	2	0.015	3	1.8844	0.0189	0.001
S7	2	0.025	3	1.8844	0.0189	0.0017
S8	2	0.050	3	1.8844	0.0189	0.0033
S9	2	0.075	3	1.8844	0.0189	0.005
S10	2	0.150	3	1.8844	0.0189	0.01

RESULTS AND DISCUSSION

The powder XRD patterns of all of the investigated samples are shown in Figure 1. The diffraction patterns in all of the samples

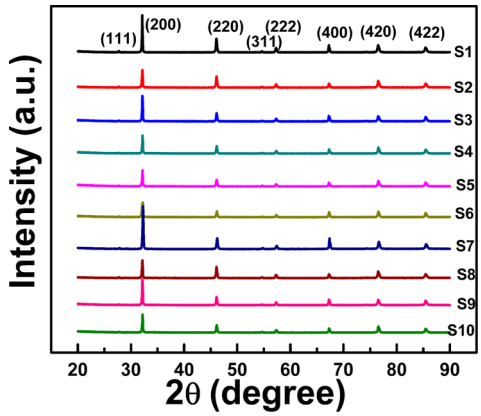

Figure 1. X-ray diffractogram of PbTe:ZnTe. It reveals the formation of the cubic phase of a rock salt (NaCl) crystal structure ($Fm\bar{3}m$ space group) in all of the samples.

reveal the formation of the cubic phase of a rock salt (NaCl) crystal structure ($Fm\bar{3}m$ space group) without any other peaks of the secondary phase. The calculated average lattice parameter for 1 and 2 mol % ZnTe contained samples is found to be lower than the lattice parameter of pure PbTe (6.462 Å) with values of 6.450 and 6.446 Å, respectively. This small contraction in the lattice parameter is due to the smaller metallic radii of Zn (1.34 Å) than that of Pb (1.75 Å).

The room temperature (300 K) values of measured electrical parameters are given in Table 2.

The negative values of the Hall coefficient and thermopower in all of the samples reveal n-type conduction in the charge-transport process. The carrier concentration (n) and mobility (μ) are calculated by the relations $n = 1/eR_H$ and $\mu = R_H/\rho$,

Table 2. Room Temperature (300 K) Values of Various Electrical Parameters in PbTe:ZnTe Samples

sample	Hall coefficient ($cm^3\ C^{-1}$)	resistivity (10^{-4} Ω·cm)	carrier concentration ($10^{19}\ cm^{-3}$)	mobility ($cm^2\ V^{-1}\ s^{-1}$)	thermopower ($\mu V\ K^{-1}$)	Fermi level position from the conduction band edge (meV)
S1	−1.41	7.75	0.44	1819	−162	31.8
S2	−0.8	6.57	0.78	1217	−135	44.7
S3	−0.35	5.51	1.79	635	−110	72.6
S4	−0.25	4.73	2.5	529	−72	87.2
S5	−0.15	3.33	4.17	450	−55	115.4
S6	−1.5	8.94	0.42	1678	−167	31
S7	−0.9	7.83	0.69	1149	−148	41.6
S8	−0.36	6.75	1.74	533	−118	71.2
S9	−0.28	5.86	2.23	478	−83	82
S10	−0.16	4.21	3.91	380	−62	111.3

respectively. The position of the Fermi level (E_F) is estimated by the nonparabolic dispersion relation[40,41] under degenerate approximation. Considering the first-order nonparabolicity only, the dispersion relation can be written as

$$\gamma(E_F) = E_F\left(1 + \frac{E_F}{E_g}\right) = \frac{\hbar^2 {k_L}^2}{2m_L} + \frac{\hbar^2 {k_T}^2}{2m_T} \quad (1)$$

where E_g is the direct energy band gap of PbTe at the L point of the Brillouin zone with a room temperature value of 0.31 eV,[41] k_L and k_T are the electron wavevectors along the longitudinal and transverse directions, respectively, $\hbar = h/2\pi$, where h is Plank's constant, and m_L and m_T are the effective masses along the longitudinal and transverse directions, respectively. For degenerate semiconductors, the carrier concentration is related to the dispersion relation as

$$n = \frac{[2m^*\gamma(E_F)]^{3/2}}{3\pi^2\hbar^3} \quad (2)$$

where m^* stands for the density-of-states effective mass and can be calculated as

$$m^* = 4^{2/3} m_e ({m_T}^2 m_L)^{1/3} = 4^{2/3} m_e[(0.16E_g)^3 \times 10.5]^{1/3} \quad (3)$$

where m_e is the electronic mass.

Figure 2 shows variation of the carrier concentration with respect to the PbI_2 content in the samples with 1 mol % ZnTe (S1−S5) and 2 mol % ZnTe (S6−S10) by square and circular symbols, respectively. The carrier concentration is found to increase linearly with the PbI_2 content in both sets of samples,

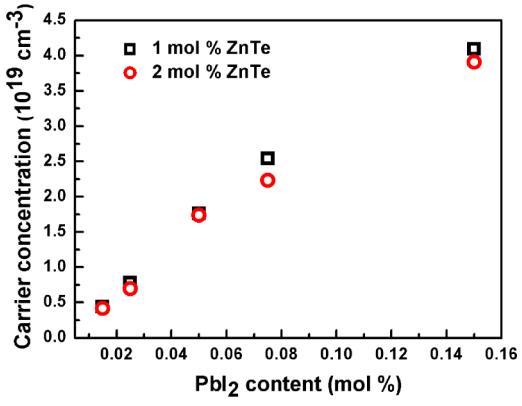

Figure 2. Variation of the carrier concentration as a function of the PbI_2 content.

which indicates the effective 1:1 doping of iodine when substituted in place of Te in PbTe. However, for the same amount of PbI_2, samples with 2 mol % ZnTe show slightly lower carrier concentrations than those of samples with 1 mol % ZnTe.

The temperature dependence of resistivity is shown in Figure 3. The monotonic rise in the resistivity with temperature indicates a typical degenerate conduction in all of the samples. The decrease in the resistivity with an increase in the PbI_2 content is due to the increased carrier concentration by the effective donor activity of iodine. As shown in Table 2, for the same PbI_2 content, the electrical resistivity in PbTe:2% ZnTe samples is found to be higher than that in the samples with 1% ZnTe. This result can be explained by the decrease in the carrier concentration (as shown in Figure 2) and loss in mobility (discussed later) in the prior set of samples (PbTe:2% ZnTe).

Figure 4 shows the temperature dependence of the Hall coefficient. The gradual rise in the Hall coefficient with temperature can be explained by the minute loss of degeneracy at higher temperatures.[31,42]

Variation of the calculated Hall mobility with temperature is shown in Figure 5. The power dependence of the mobility with temperature, i.e., $\mu \sim T^{-\delta}$, has been observed for all of the samples. The average value of the exponent (δ) is found to be 2.3 for the samples with 1 mol % ZnTe and 1.9 for the samples with 2 mol % ZnTe. These values of δ denote the domination of acoustic phonon scattering in the charge-carrier transport at higher temperatures.[43] The mobility in samples with 2 mol % ZnTe is found to be lower than that of samples with 1 mol % ZnTe.

The temperature-dependent thermopower is shown in Figure 6. The nearly linear temperature dependence of thermopower indicates typical degenerate conduction in all of the samples throughout the investigated temperature range, and it is consistent with the temperature-dependent resistivity. The inverse relationship between the thermopower and carrier concentration can easily be observed from Table 2; i.e., with a rise in the carrier concentration, the thermopower decreases. The monotonic decrease in the thermopower with the carrier concentration indicates single-band transport in the material system.[15]

The room temperature values of the thermopower are compared with the theoretical Pisarenko line[44] of n-type PbTe under single parabolic band approximation (SPB) and domination of acoustic phonon scattering with an electron density-of-state mass (m^*) value of $0.25m_e$,[42,45] as shown in Figure 7. The room temperature thermopower is found to be in

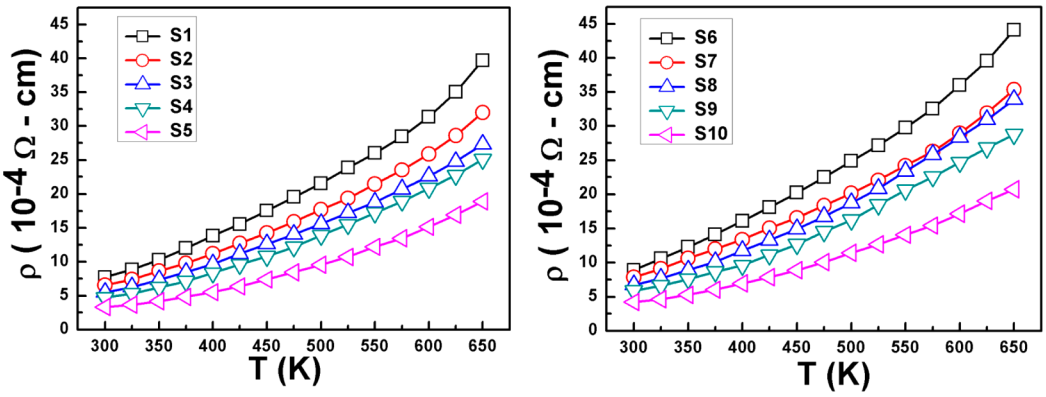

Figure 3. Temperature-dependent resistivity. The monotonic rise in the resistivity with temperature indicates typical degenerate conduction in all of the samples.

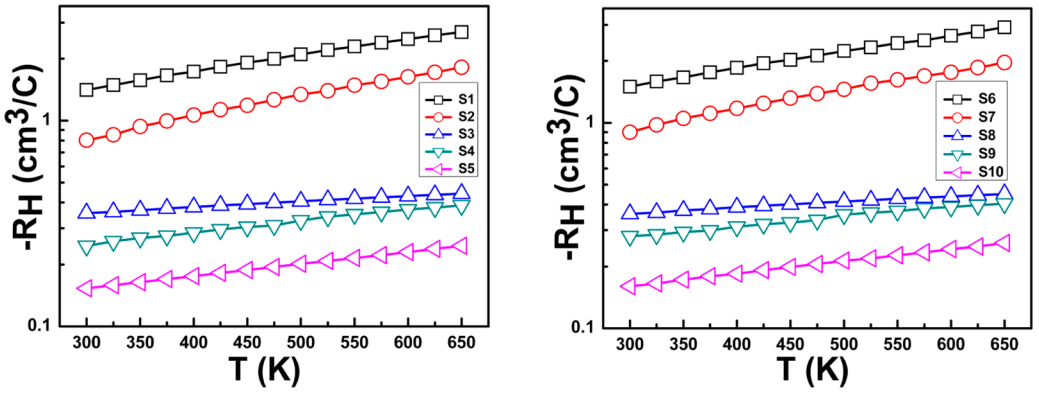

Figure 4. Temperature-dependent Hall coefficients.

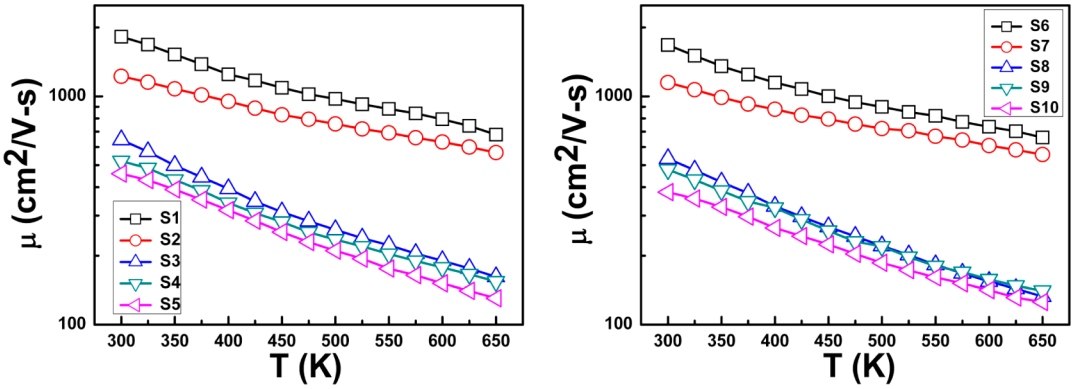

Figure 5. Variation of the calculated Hall mobility with temperature.

good agreement with the theoretical plot. This shows no enhancement in the thermopower that might be attributed to the modified density-of-states in PbTe by Zn resonant states.[28] The position of such resonant states of Zn (if it exists at all) cannot be accessed by the obtained values of the carrier concentration in the present study, or maybe the width of the modified density-of-states is not sufficiently wide to be able to locate the Fermi level inside the modified region (although narrow width leads to higher thermopower, because of the experimental limitations over sample and defect chemistry, a sufficient width (10−100 meV) of the modified density-of-states is required[46]). The calculated values of the Fermi level (Table 2) suggest that the resonant states of Zn should have situated above 115.4 meV from the conduction band edge (if exists at all and is accessible in reality). Further investigation is required to estimate the exact location of Zn resonant states and the width of the modified density-of-states in PbTe, which will then ensure whether it could practically be accessed and utilized for enhancement of the thermopower under a feasible carrier concentration limit and temperature dependence of the electronic band structure. However, for complete exploitation of the resonance levels in thermoelectrics, two other conditions need to be fulfilled and are as follows: (i) the resonant level must involve charge conduction; i.e., it should not trap the charge carriers; (ii) the background density-of-states should be minimal.[46] Previous reports such as Tl resonance in the PbTe valence band[28] and Sn in Bi_2Te_3[30] have been found to fulfill the

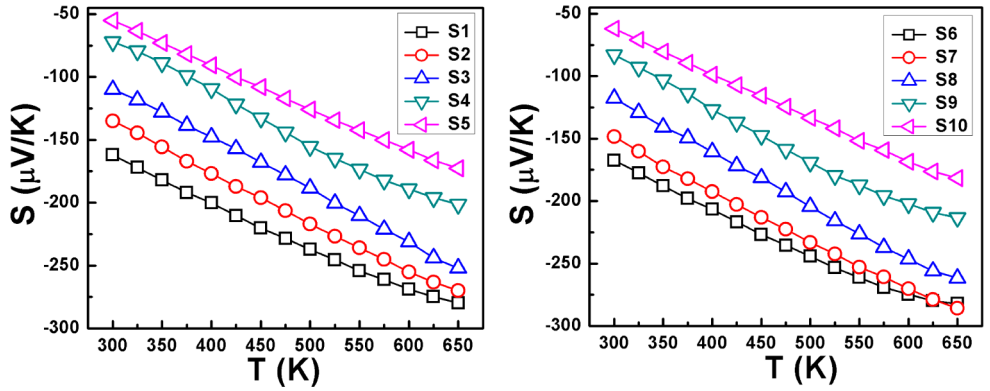

Figure 6. Temperature-dependent thermopower. The linear rise in the thermopower with temperature indicates typical degenerate conduction in all of the samples.

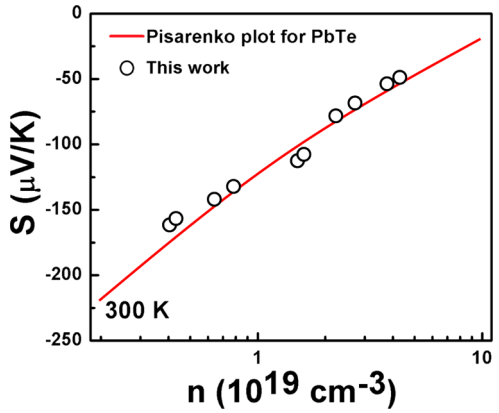

Figure 7. Theoretical Pisarenko line of PbTe at 300 K, with room temperature values of the thermopower in all of the samples (circular symbols).

above criteria, and as a result, significant enhancement has been observed in zT in these systems.

The temperature dependence of the power factor (S^2/ρ) is shown in Figure 8. The maximum power factor values and the corresponding temperatures in all of the samples are given in Table 3.

Figure 9 shows the temperature-dependent thermal diffusivity in all of the samples. The thermal diffusivity is found to increase with a rise in the PbI_2 content due to increased carrier concentrations at higher doping levels. The

Table 3. Maximum Power Factor Values and the Corresponding Temperatures in All of the Samples

sample	maximum power factor (10^{-4} W m^{-1} K^{-2})	temperature (K)
S1	33.88	300
S2	28.45	375
S3	23.99	625
S4	17.53	525
S5	16.82	525
S6	31.36	300
S7	28.08	325
S8	22.37	525
S9	17.59	500
S10	16.54	600

measured value of the specific heat is found to be nearly temperature-independent in both sets of samples with average values of 0.162 and 0.163 J g^{-1} K^{-1} respectively for the samples with 1 and 2 mol % ZnTe. The average deviations in the measured specific heat from the empirical relation given in ref 42 are found to be 2.5 and 3.1% respectively for the samples with 1 and 2 mol % ZnTe. The average densities of the samples with 1 and 2 mol % ZnTe are measured to be 8.101 and 8.083 g cm^{-3}, respectively.

The temperature dependence of the total and lattice thermal conductivity is shown in Figure 10. The lattice part of the total thermal conductivity (lattice thermal conductivity, κ_l) is estimated as $\kappa_l = \kappa - \kappa_e$, where κ_e is the electronic thermal

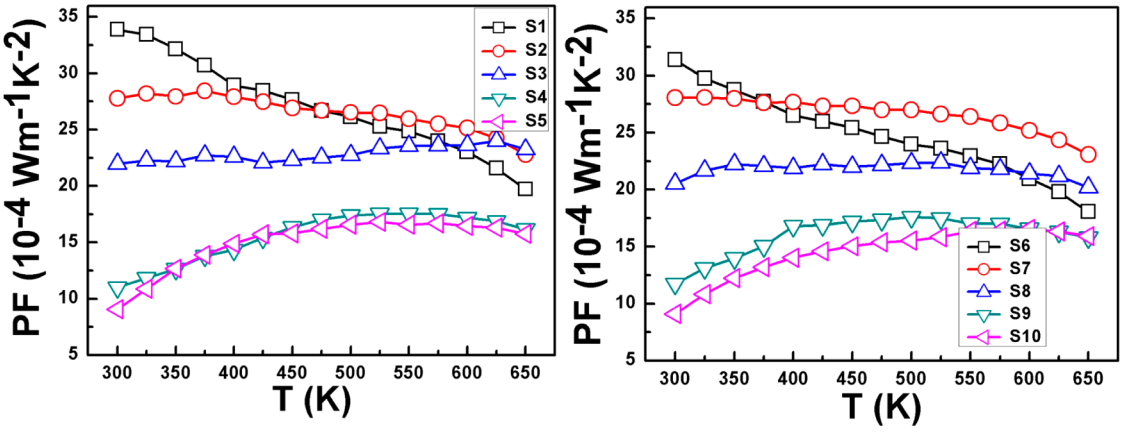

Figure 8. Temperature dependence of the power factor in all of the samples.

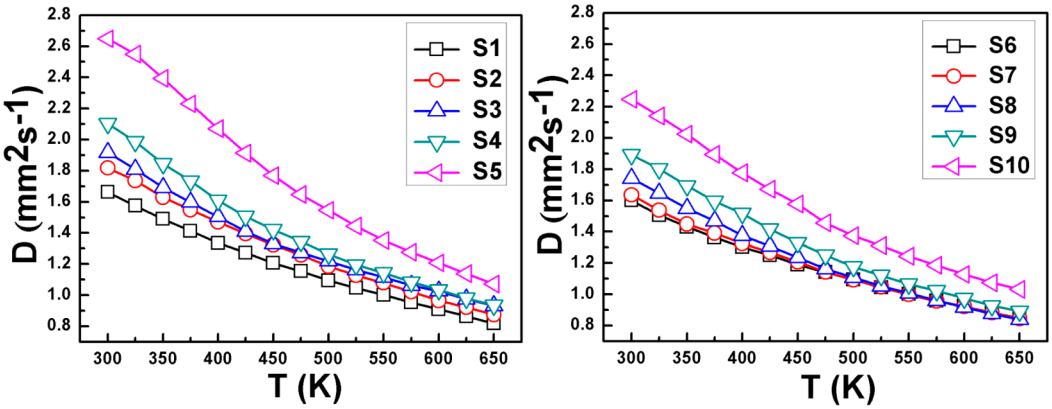

Figure 9. Temperature-dependent thermal diffusivity in PbTe:ZnTe.

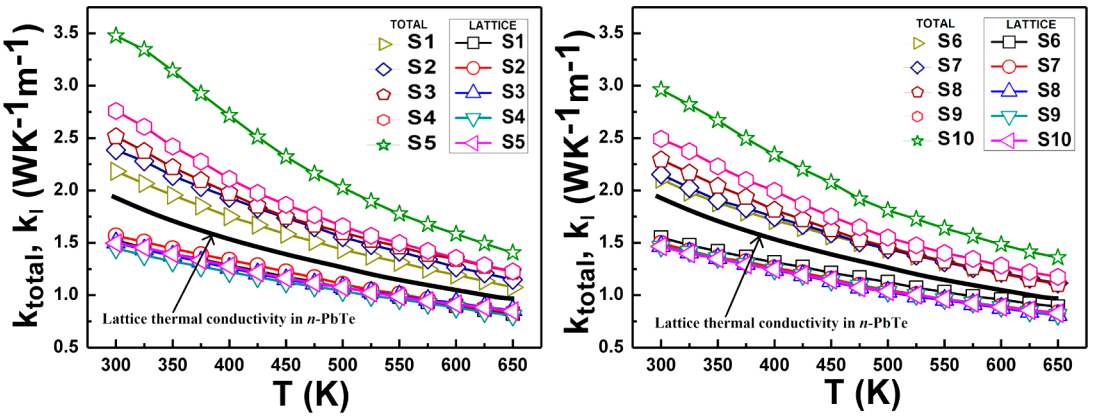

Figure 10. Temperature dependence of the total and lattice thermal conductivity.

conductivity. The electronic part of the total thermal conductivity is calculated as $\kappa_e = LT/\rho$, where L is the Lorenz number. The temperature-dependent Lorenz number is estimated using the SPB model under acoustic phonon limited scattering as[47−49]

$$L = \frac{{k_B}^2}{e^2}\left[\frac{\left(r+\frac{7}{2}\right)F_{r+5/2}(\eta)}{\left(r+\frac{3}{2}\right)F_{r+1/2}(\eta)} - \left(\frac{\left(r+\frac{5}{2}\right)F_{r+3/2}(\eta)}{\left(r+\frac{3}{2}\right)F_{r+1/2}(\eta)}\right)^2\right] \quad (4)$$

where $F_n(\eta) = \int_0^\infty(\omega^n)/[1+\exp(\omega-\eta)]\,d\omega$ is the nth order Fermi integral, η is the reduced Fermi energy ($=E_F/kT$), k_B is Boltzmann's constant, and r is the scattering parameter ($=-^1/_2$ for the acoustic phonon scattering approximation). The reduced Fermi energy is derived from the thermopower values using the following relation:

$$S = \frac{k_B}{e}\left(\frac{\left(r+\frac{5}{2}\right)F_{r+3/2}(\eta)}{\left(r+\frac{3}{2}\right)F_{r+1/2}(\eta)} - \eta\right) \quad (5)$$

The calculated Lorenz numbers are found to be in the range 1.53×10^{-8}–2.19×10^{-8} W Ω K^{-2}. The estimated room temperature lattice thermal conductivity in all of the samples is found to be <1.6 W m^{-1} K^{-1}, which is significantly lower than that in pristine PbTe.[13,27,50,51] The black solid line in Figure 10 shows the lattice thermal conductivity in our grown n-type pristine PbTe (because κ_l is independent of the doping type, it would be the same for p-type pristine PbTe). The average percentage reductions in the lattice thermal conductivity at 300 and 650 K are found to be 21% and 30%, respectively. The lower values of κ_l indicate significant enhancement of the scattering of long-wavelength phonons in PbTe by Zn substitution, which plays a major role in thermal conduction in solids.

Figure 11a shows the low-magnification bright-field HRTEM micrograph of the PbTe:2% ZnTe sample. The micrograph reveals various nanoscale secondary phases of ZnTe (dark contrast regions) in the host PbTe matrix. Although it is very difficult to get actual quantitative chemical compositions of the embedded nanostructures because of overlap with the host matrix, energy-dispersive X-ray spectroscopy (EDS) measurements have been performed to confirm the Zn and Te contents in the nanostructures (shown in the Supporting Information, section SI-2). The presence of such a nanoscale phase in the parent matrix is known for reduction in the lattice thermal conductivity of the host material by long-wavelength phonon scattering.[52,53] Because of the formation of such nanostructures, the lattice thermal conductivity in the present system is found to be lower than that of pristine PbTe. Similar nanostructures have been found in PbTe:1% ZnTe (shown in Supporting Information, section SI-3). However, the density of the nanostructures in PbTe:1% ZnTe is found to be lower than that of the sample with 2% ZnTe. Parts b and c of Figure 11 show the high-magnification HRTEM images of a selected portion. The coherent nature of the embedded nanostructures (of size distribution between 2 and 9 nm) with the host matrix of PbTe is observed. The coherent nature of the embedded nanostructures implies a rock salt crystal structure of ZnTe,

dx.doi.org/10.1021/am405410e | ACS Appl. Mater. Interfaces 2014, 6, 3995−4004

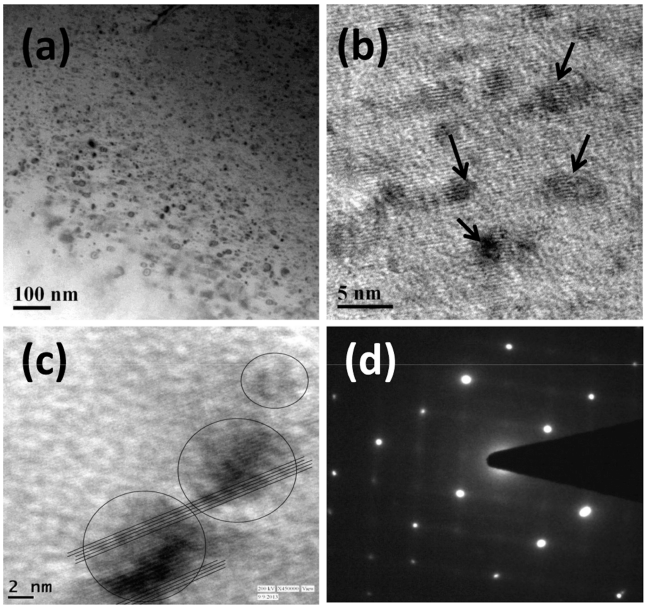

Figure 11. (a) Low-magnification bright-field HRTEM micrograph of the PbTe:2% ZnTe sample (S6). (b) High-magnification HRTEM image of a selected portion of the PbTe:2% ZnTe sample (S6). (c) Coherent nature of the interface between the nanostructures and the matrix. (d) SAED pattern.

although in normal temperature and pressure, it exists in the zinc blende form. The sharp diffraction spots without any splitting in the SAED pattern (Figure 11d) confirm complete alignment in the crystallographic planes and directions between the two phases. The coherent nature of the ZnTe nanostructures in the PbTe matrix is a consequence of almost similar lattice constants of PbTe (6.462 Å) and ZnTe (6.103 Å). The formation of such nanostructures was possible because of the very low solubility of Zn in PbTe.[54] XRD (Figure 1) did not show any peak of the ZnTe phase, but it indeed exhibited a slight contraction in the lattice parameter in the PbTe matrix, an indication of the substitution of Zn at Pb sites. However, as discussed above, TEM studies showed the presence of a secondary phase in the host matrix, which suggests that the solubility estimation of an element in the parent material system by XRD is not always correct.[35]

Figure 12a shows the band diagram of the PbTe−ZnTe−PbTe interface drawn according to the electron affinity rule, with the vacuum level used as a reference.[55] Figure 12b shows quantum tunneling of the charge carriers through a narrow depletion width at the heterojunction. The electron affinities (χ) for PbTe and ZnTe are reported as 4.6 and 3.53 eV, respectively;[56,57] therefore, an energy barrier (E_B) of height 1.07 eV exists between the conduction band extremes of PbTe and ZnTe. (In the calculations, ZnTe is considered to be a zinc blende crystal structure. However, in the present investigation, it is found to be a rock salt structure. So, the values of χ, etc., could have been different, which, in turn, could affect the height of the barrier.) This barrier could alter the value of the carrier mobility as found in the literature.[14,15,58,59] The carrier-concentration-dependent mobility in all of the samples along with the pristine (without Zn) PbI_2-doped PbTe is shown in Figure 13.

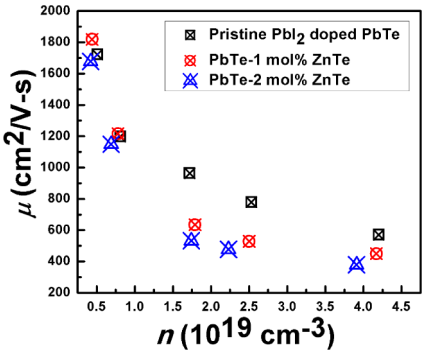

Figure 13. Variation of the room temperature mobility with the carrier concentration in pristine PbTe (black symbols), PbTe−1 mol % ZnTe (red symbols), and PbTe−2 mol % ZnTe (blue symbols).

At lower carrier concentrations (S1, S2, S6, and S7), for similar n, the calculated mobility in our samples is found to be slightly reduced from that of the pristine PbTe. This finding suggests that the carrier mobility is not affected much by the band offset. The size of the foreign phase nanostructures within the host matrix, width of the depletion region at the heterojunction (in the present case formed by PbTe and ZnTe), and nature of the interface between the different phases play a crucial role in the carrier mobility. For the carrier mobility to remain at least unaffected, quantum effects could play a dominant role in carrier transport, which is possible if the size of the nanostructure is comparable with the Bohr exciton radius and the depletion width becomes small enough such that it is transparent to charge carriers. However, the effect of carrier−phonon scattering on the mobility could not be neglected. Otherwise, the carriers may bounce back or scatter, resulting in an appreciable loss in mobility. In the present case, the sizes of the ZnTe nanostructures are typically found to be

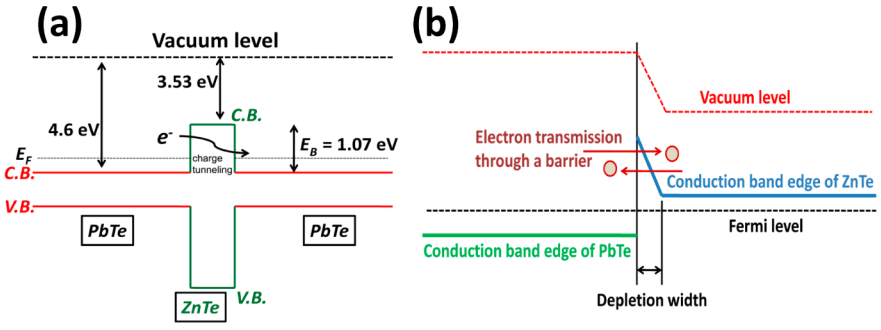

Figure 12. (a) Band diagram of the PbTe−ZnTe−PbTe interface showing charge-carrier tunneling through an energy barrier. (b) Quantum tunneling of the charge carriers through a narrow depletion width at the heterojunction.

between 2 and 9 nm and the calculated depletion width [using thermionic emission theory (details are given in the Supporting Information, section SI-4)] at the heterojunction is found to be negligible in comparison to the electron wavelength in the solid. These dimensions suggest a distinct possibility of quantum tunneling of the charge carriers over the energy barrier (as shown in Figure 12). Moreover, the coherent nature of the interface allows resistance-less conduction of the charge carriers between different phases. As discussed earlier, Figure 12 depicts two possibilities of charge tunneling through a barrier, viz., (a) direct tunneling through the ZnTe nanostructure and (b) tunneling through a narrow depletion layer at the heterojunction between PbTe and ZnTe. For the tunneling shown in Figure 12b, only electrons of energy $E > E_F$ can tunnel through the depletion width into the conduction band of ZnTe, which would cause a loss in the overall mobility. However, for the tunneling shown in Figure 12a, electrons of energy $E \sim E_F$ can also tunnel through the barrier (ZnTe nanostructure) along with high-energy electrons ($E > E_F$), which indicates domination of this tunneling in the transport process.

At higher carrier concentrations, a significant reduction in the mobility has been observed. Such a reduction in the mobility could be due to the enhanced density-of-states (thus increased carrier effective mass) by Zn resonant states,[28] but the strong agreement between the room temperature thermopower and the theoretical Pisarenko line (shown in Figure 7 in the manuscript) summarily refutes this prediction.

The reason for such a reduction in the mobility at a higher carrier concentration range could be due to the enhanced probability of carrier−phonon scattering followed by carrier−carrier scattering at the heterojunction,[60] which is schematically shown in Figure 14. Such scattering mechanisms change the carrier trajectory, which imposes an obstruction in the smooth tunneling of the charge carriers[58,60] and thereby affects the mobility. With reference to the PbTe−SrTe system,[14] where there exists no band offset (no potential barrier) between the PbTe matrix and the embedded SrTe endotaxial nanostructures, such a mobility reduction at higher carrier concentration (~5.4 × 10^{19} cm^{-3}) has not been observed. This observation further indicates the existence of potential barriers at the PbTe−ZnTe heterojunction.

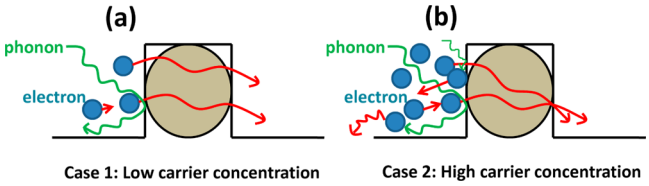

Figure 14. Charge-carrier tunneling through a barrier (a) without domination of carrier−phonon and carrier−carrier scattering and (b) with domination of carrier−phonon and carrier−carrier scattering at the heterojunction.

Because of the increased density of embedded nanostructures of ZnTe in PbTe−2 mol % ZnTe than that of PbTe−1 mol % ZnTe, the increased probability of carrier−phonon and carrier−carrier scattering results in slightly reduced carrier mobility in the prior set of samples, which decreases further across the board for every PbI_2 doping level. Also, the scattered carriers by such scattering mechanisms could not contribute completely to the Hall effect; thus, the calculated carrier concentration in 2 mol % Zn samples is found to be slightly lower than that of samples with 1 mol % Zn.[23,58,59]

The temperature-dependent figure of merit in all of the samples is shown in Figure 15. Maximum zT values of 1.29 and 1.35 are found in samples S2 and S7 at 650 K, respectively. These values are found to be higher than those of our grown reference samples of I-doped PbTe at this temperature of similar carrier concentration (0.75 × 10^{19} cm^{-3}), which indicates a notable enhancement in zT by thermal conductivity reduction via ZnTe coherent nanostructures. The maximum zT value of the reference sample is found to be 1.12 at 625 K (details are given in the Supporting Information, section SI-5), which is ~13% and ~17% less than those of S2 and S7, respectively. In ref 42, the sample with a carrier concentration of ~2 × 10^{19} cm^{-3} shows a maximum zT value of ~1.3 at 650 K, and samples with carrier concentrations of ~0.5 × 10^{19} and ~1 × 10^{19} cm^{-3} show maximum zT values of 0.9 at 620 K and 1.2 at 680 K, respectively. Samples S1, S3, S6, and S8 also show zT values greater than 1 in a wider temperature range at higher temperatures.

CONCLUSION

For experimental observation of the theoretically predicted Zn resonance states and their effect on the thermoelectric properties in PbTe, thermoelectric transport in PbI_2-doped PbTe:ZnTe has been investigated. The negative values of the Hall coefficient and thermopower in all of the samples revealed n-type conduction in the charge-transport process. The monotonic rise in the resistivity and thermopower with temperature indicated typical degenerate conduction in all of

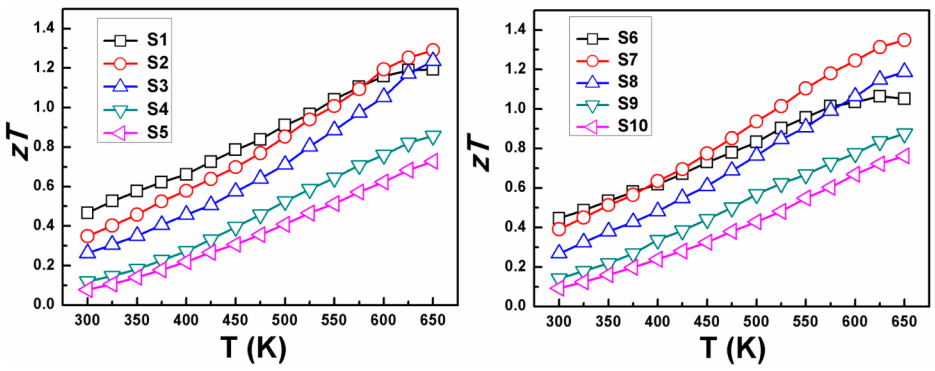

Figure 15. Temperature-dependent figure of merit in all of the samples. The maximum zT value of 1.35 is observed in sample S7 at 650 K.

the samples. The room temperature values of the thermopower do not show any evidence of Zn resonanace states at least up to a carrier concentration of 4.17×10^{19} cm^{-3}. Thus, either there exists no such resonant states, or they could not be accessed by the obtained values of the carrier concentration in the present study, or the width of the modified density-of-states is not sufficiently wide to be able to locate the Fermi level inside the modified region. Because of the low solubility of Zn in PbTe, a phase of coherent ZnTe nanostructures of size 2−9 nm has been found in the host matrix of PbTe. A significant reduction in the lattice thermal conductivity has been observed because of the enhanced scattering of long-wavelength phonons by these ZnTe nanostructures. The reduced lattice thermal conductivity enabled significant enhancement in the figure of merit in the present investigation over I-doped pristine PbTe. The coherent boundary between the ZnTe−PbTe interface along with the narrow band offset and depletion width allows resistance-less transmission of charge carriers at lower carrier concentrations through different phases, for which the carrier mobility remains unaffected. The carrier−phonon and carrier−carrier scattering at the heterojunction are found to dominate strongly at higher carrier concentrations and slightly at higher Zn content, due to which a reduced mobility has been observed.

■ ASSOCIATED CONTENT

Supporting Information

Homogeneity analysis of the torch melted sample by comparative analysis of various room temperature (300 K) thermoelectric parameters in conventionally grown and torch-melted 0.05 mol % PbI_2-doped PbTe, EDS spectra to examine the presence of Zn and Te content in the nanostructures, low-magnification bright-field HRTEM micrograph of PbTe for 1% ZnTe and 2% ZnTe samples, details of the thermionic emission theory relevant to this study, and comparative plots of various measured electrical parameters in samples S2 and S7 with the grown reference samples of I-doped PbTe (of carrier concentration 0.75×10^{19} cm^{-3}). This material is available free of charge via the Internet at http://pubs.acs.org.

■ AUTHOR INFORMATION

Corresponding Author

*E-mail: pallab@matsc.iitkgp.ernet.in.

Notes

The authors declare no competing financial interest.

■ ACKNOWLEDGMENTS

P.K.R. acknowledges financial support from CSIR through CSIR NET. The authors acknowledge help from the Department of Metallurgical and Materials Engineering, IIT Kharagpur, for the thermal conductivity measurements.

■ REFERENCES

(1) Rowe, D. M. *CRC Handbook of Thermoelectrics*; CRC Press: Boca Raton, FL, 1995.

(2) LaLonde, A. D.; Pei, Y.; Wang, H.; Snyder, G. J. Lead Telluride Alloy Thermoelectrics. *Mater. Today* **2011**, *14*, 526−532.

(3) Snyder, G. J.; Toberer, E. S. Complex Thermoelectric Materials. *Nat. Mater.* **2008**, *7*, 105−114.

(4) Bell, L. E. Cooling, Heating, Generating Power, and Recovering Waste Heat with Thermoelectric Systems. *Science* **2008**, *321*, 1457−1461.

(5) Harman, T. C.; Taylor, P. J.; Walsh, M. P.; LaForge, B. E. Quantum Dot Superlattice Thermoelectric Materials and Devices. *Science* **2002**, *297*, 2229−2232.

(6) Zhang, Q.; He, J.; Zhu, T. J.; Zhang, S. N.; Zhao, X. B.; Tritt, T. M. High Figures of Merit and Natural Nanostructures in $Mg_2Si_{0.4}Sn_{0.6}$ Based Thermoelectric Materials. *Appl. Phys. Lett.* **2008**, *93*, 102109−102112.

(7) Ioffe, A. *Semiconductor Thermoelements and Thermoelectric Cooling*; Infosearch: London, 1957.

(8) Dresselhaus, M. S.; Chen, G.; Tang, M. Y.; Yang, R. G.; Lee, H.; Wang, D. Z.; Ren, Z. F.; Fleurial, J. P.; Gogna, P. New Directions for Low-Dimensional Thermoelectric Materials. *Adv. Mater.* **2007**, *19*, 1043−1053.

(9) Zhang, Q.; Zhang, Q.; Chen, S.; Liu, W.; Lukas, K.; Yan, X.; Wang, H.; Wang, D.; Opeil, C.; Chen, G.; Ren, Z. Suppression of Grain Growth by Additive in Nanostructured *p*-type Bismuth Antimony Tellurides. *Nano Energy* **2012**, *1*, 183−189.

(10) Scheele, M.; Oeschler, N.; Meier, K.; Kornowski, A.; Linke, C.; Weller, H. Synthesis and Thermoelectric Characterization of Bi_2Te_3 Nanoparticles. *Adv. Funct. Mater.* **2009**, *19*, 3476−3483.

(11) Heremans, J. P.; Thrush, C. M.; Morelli, D. T. Thermopower Enhancement in Lead Telluride Nanostructures. *Phys. Rev. B* **2004**, *70*, 115334−115339.

(12) Han, M.; Hoang, K.; Kong, H.; Pcionek, R.; Uher, C.; Paraskevopoulos, K. M.; Mahanti, S. D.; Kanatzidis, M. G. Substitution of Bi for Sb and its Role in the Thermoelectric Properties and Nanostructuring in $Ag_{1-x}Pb_{18}MTe_{20}$ (M = Bi, Sb) (x = 0, 0.14, 0.3). *Chem. Mater.* **2008**, *20*, 3512−3520.

(13) Poudeu, P. F. P.; D'Angelo, J.; Kong, H.; Downey, A.; Short, J. L.; Pcionek, R.; Hogan, T. P.; Uher, C.; Kanatzidis, M. G. Nanostructures Versus Solid Solutions: Low Lattice Thermal Conductivity and Enhanced Thermoelectric Figure of Merit in $Pb_{9.6}Sb_{0.2}Te_{10-x}Se_x$ Bulk Materials. *J. Am. Chem. Soc.* **2006**, *128*, 14347−14355.

(14) Biswas, K.; He, J.; Zhang, Q.; Wang, G.; Uher, C.; Dravid, V. P.; Kanatzidis, M. G. Strained Endotaxial Nanostructures with High Thermoelectric Figure of Merit. *Nat. Chem.* **2011**, *3*, 160−166.

(15) Rawat, P. K.; Paul, B.; Banerji, P. Thermoelectric Properties of $PbSe_{0.5}Te_{0.5}$:$x(PbI_2)$ with Endotaxial Nanostructures: A Promising *n*-type Thermoelectric Material. *Nanotechnology* **2013**, *24*, 215401−215408.

(16) Ohta, M.; Biswas, K.; Lo, S.; He, J.; Chung, D. Y.; Dravid, V. P.; Kanatzidis, M. G. Enhancement of Thermoelectric Figure of Merit by the Insertion of MgTe Nanostructures in *p*-Type PbTe Doped with Na_2Te. *Adv. Energy Mater.* **2012**, *2*, 1117−1123.

(17) Jiaqing, H.; Kanatzidis, M. G.; Dravid, V. P. High Performance Bulk Thermoelectrics Via Panoscopic Appraoch. *Mater. Today* **2013**, *16*, 166−176.

(18) Wang, H.; LaLonde, A. D.; Pei, Y.; Snyder, G. J. The Criteria for Beneficial Disorder in Thermoelectric Solid Solutions. *Adv. Funct. Mater.* **2013**, *23*, 1586−1596.

(19) Zhao, L.; Dravid, V. P.; Kanatzidis, M. G. The Panoscopic Approach to High Performance Thermoelectrics. *Energy Environ. Sci.* **2014**, *7*, 251−268.

(20) Li, J.; Liu, W.; Zhao, L.; Zhou, M. High-Performance Nanostructured Thermoelectric Materials. *NPG Asia Mater.* **2010**, *2*, 152−158.

(21) Zebarjadi, M.; Joshi, G.; Zhu, G. H.; Yu, B.; Minnich, A.; Lan, Y. C.; Wang, X. W.; Dresselhaus, M.; Ren, Z. F.; Chen, G. Power Factor Enhancement by Modulation Doping in Bulk Nanocomposites. *Nano Lett.* **2011**, *11*, 2225−2230.

(22) Yu, B.; Zebarjadi, M.; Wang, H.; Lukas, K.; Wang, H.; Wang, D.; Opeil, C.; Dresselhaus, M.; Chen, G.; Ren, Z. Enhancement of Thermoelectric Properties by Modulation-Doping in Silicon Germanium Alloy Nanocomposites. *Nano Lett.* **2012**, *12*, 2077−2082.

(23) Martin, J.; Wang, L.; Chen, L. D.; Nolas, G. S. Enhanced Seebeck Coefficient through Energy-Barrier Scattering in PbTe Nanocomposites. *Phys. Rev. B* **2009**, *79*, 115311−115315.

(24) Pei, Y.; LaLonde, A. D.; Heinz, N. A.; Shi, X.; Iwanaga, S.; Wang, H.; Chen, L.; Snyder, G. J. Stabilizing the Optimal Carrier Concentration for High Thermoelectric Efficiency. *Adv. Mater.* **2011**, *23*, 5674−5678.
(25) Rawat, P. K.; Paul, B.; Banerji, P. An Alternative Approach for Optimal Carrier Concentration Towards Ideal Thermoelectric Performance. *Phys. Status Solidi RRL* **2012**, *6*, 481−483.
(26) Pei, Y.; May, A. F.; Snyder, G. J. Self-Tuning the Carrier Concentration of PbTe/Ag_2Te Composites with Excess Ag for High Thermoelectric Performance. *Adv. Energy Mater.* **2011**, *1*, 291−296.
(27) Pei, Y.; LaLonde, A.; Iwanaga, S.; Snyder, G. J. High Thermoelectric Figure of Merit in Heavy Hole Dominated PbTe. *Energy Environ. Sci.* **2011**, *4*, 2085−2089.
(28) Heremans, J. P.; Jovovic, V.; Toberer, E. S.; Saramat, A.; Kurosaki, K.; Charoenphakdee, A.; Yamanaka, S.; Snyder, G. J. Enhancement of Thermoelectric Efficiency in PbTe by Distortion of the Electronic Density of States. *Science* **2008**, *321*, 554−557.
(29) Zhang, Q.; Wang, H.; Liu, W.; Wang, H.; Yu, B.; Zhang, Q.; Tian, Z.; Ni, G.; Lee, S.; Esfarjani, K.; Chen, G.; Ren, Z. Enhancement of Thermoelectric Figure-of-Merit by Resonant States of Aluminium Doping in Lead Selenide. *Energy Environ. Sci.* **2012**, *5*, 5246−5251.
(30) Jaworski, C. M.; Kulbachinskii, V.; Heremans, J. P. Resonant Level Formed by Tin in Bi_2Te_3 and The Enhancement of Room-Temperature Thermoelectric Power. *Phys. Rev. B* **2009**, *80*, 233201−233204.
(31) Rawat, P. K.; Paul, B.; Banerji, P. Impurity-Band Induced Transport Phenomenon and Thermoelectric Properties in Yb Doped $PbTe_{1-x}I_x$. *Phys. Chem. Chem. Phys.* **2013**, *15*, 16686−16692.
(32) König, J. D.; Nielsen, M. D.; Gao, Y.; Winkler, M.; Jacquot, A.; Böttner, H.; Heremans, J. P. Titanium Forms a Resonant Level in the Conduction Band of PbTe. *Phys. Rev. B* **2011**, *84*, 205126−205130.
(33) Jovovic, V.; Thiagarajan, S. J.; Heremans, J. P.; Komissarova, T.; Khoklov, D. R.; Nicorici, A. Low Temperature Thermal, Thermoelectric, and Thermomagnetic Transport in Indium Rich $Pb_{1-x}Sn_xTe$ Alloys. *J. Appl. Phys.* **2008**, *103*, 053710−053717.
(34) Ahmad, S.; Mahanti, S. D.; Hoang, K.; Kanatzidis, M. G. *Ab initio* Studies of the Electronic Structure of Defects in PbTe. *Phys. Rev. B* **2006**, *74*, 155205−155217.
(35) Ahn, K.; Han, M.; He, J.; Androulakis, J.; Ballikaya, S.; Uher, C.; Dravid, V. P.; Kanatzidis, M. G. Exploring Resonance Levels and Nanostructuring in the PbTe−CdTe System and Enhancement of the Thermoelectric Figure of Merit. *J. Am. Chem. Soc.* **2010**, *132*, 5227−5235.
(36) Jaworski, C. M.; Heremans, J. P. Thermoelectric Transport Properties of the *n*-Type Impurity Al in PbTe. *Phys. Rev. B* **2012**, *85*, 033204−033206.
(37) Borup, K. A.; Toberer, E. S.; Zoltan, L. D.; Nakatsukasa, G.; Errico, M.; Fleurial, J. P.; Iversen, B. B.; Snyder, G. J. Measurement of the Electrical Resistivity and Hall Coefficient at High Temperatures. *Rev. Sci. Instrum.* **2012**, *83*, 123902−123908.
(38) Paul, B. Simple Apparatus for the Multipurpose Measurements of Different Thermoelectric Parameters. *Measurement* **2012**, *45*, 133−139.
(39) Ponnambalam, V.; Lindsey, S.; Hickman, N. S.; Tritt, T. M. Sample Probe to Measure Resistivity and Thermopower in the Temperature Range of 300−1000 K. *Rev. Sci. Instrum.* **2006**, *77*, 073904−073908.
(40) Jovovic, V.; Thiagarajan, S. J.; West, J.; Heremans, J. P.; Story, T.; Golacki, Z.; Paszkowicz, W.; Osinniy, V. Transport and Magnetic Properties of Dilute Rare-Earth−PbSe Alloys. *J. Appl. Phys.* **2007**, *102*, 043707−043712.
(41) Akimov, B. A.; Dmitriev, A. V.; Khokhlov, D. R.; Ryabova, L. I. Carrier Transport and Non-Equilibrium Phenomena in Doped PbTe and Related Materials. *Phys. Status Solidi A* **1993**, *137*, 9−55.
(42) LaLonde, A. D.; Pei, Y.; Snyder, G. J. Reevaluation of $PbTe_{1-x}I_x$ as High Performance n-Type Thermoelectric Material. *Energy Environ. Sci.* **2011**, *4*, 2090−2096.
(43) Allgaier, R. S.; Scanlon, W. W. Mobility of Electrons and Holes in PbS, PbSe, and PbTe Between Room Temperature and 4.2 K. *Phys. Rev.* **1958**, *111*, 1029−1037.
(44) Ravich, Y.; Efimova, B.; Smirnov, I. *Semiconducting Lead Chalcogenides*; Plenum: New York, 1970.
(45) Wang, H.; Charoenphakdee, A.; Kurosaki, K.; Yamanaka, S.; Snyder, G. J. Reduction of Thermal Conductivity in PbTe:Tl by Alloying with $TlSbTe_2$. *Phys. Rev. B: Condens. Matter Mater. Phys.* **2011**, *83*, 024303−024307.
(46) Heremans, J. P.; Wiendlocha, B.; Chamoire, A. M. Resonant Levels in Bulk Thermoelectric Semiconductors. *Energy Environ. Sci.* **2012**, *5*, 5510−5530.
(47) Zhao, L.; Lo, S.; He, J.; Li, H.; Biswas, K.; Androulakis, J.; Wu, C.; Hogan, T. P.; Chung, D. Y.; Dravid, V. P.; Kanatzidis, M. G. High Performance Thermoelectrics from Earth-Abundant Materials: Enhanced Figure of Merit in PbS by Second Phase Nanostructures. *J. Am. Chem. Soc.* **2011**, *133*, 20476−20487.
(48) Lioutas, C. B.; Frangis, N.; Todorov, I.; Chung, D. Y.; Kanatzidis, M. G. Understanding Nanostructures in Thermoelectric Materials: An Electron Microscopy Study of $AgPb_{18}SbSe_{20}$ Crystals. *Chem. Mater.* **2010**, *22*, 5630−5635.
(49) Fistul', V. I. *Heavily Doped Semiconductors*; Plenum: New York, 1969.
(50) Pie, Y.; Lensch-Falk, L.; Toberer, E. S.; Medlin, D. L.; Snyder, G. J. High Thermoelectric Performance in PbTe Due to Large Nanoscale Ag_2Te Precipitates and La Doping. *Adv. Funct. Mater.* **2011**, *21*, 241−249.
(51) Sootsman, J. R.; Pcionek, R. J.; Kong, H.; Uher, C.; Kanatzidis, M. G. Strong Reduction of Thermal Conductivity in Nanostructured PbTe Prepared by Matrix Encapsulation. *Chem. Mater.* **2006**, *18*, 4993−4995.
(52) Kanatzidis, M. G. Nanostructured Thermoelectrics: The New Paradigm? *Chem. Mater.* **2010**, *22*, 648−659.
(53) Tian, Z.; Garg, J.; Esfarjani, K.; Shiga, T.; Shiomi, J.; Chen, G. Phonon Conduction in PbSe, PbTe, and $PbTe_{1-x}Se_x$ from First-Principles Calculations. *Phys. Rev. B* **2012**, *85*, 184303−184309.
(54) Vydyanath, H. R. Defect Structure of Zn-Doped PbTe. *J. Appl. Phys.* **1976**, *47*, 5010−5015.
(55) Neamen, D. A. *Semiconductor Physics and Devices*; The McGraw Hill Co.: New Delhi, India, 2007.
(56) Nill, K. W.; Calawa, A. R.; Harman, T. C.; Walpole, J. N. Laser Emission from Metal Semiconductor Barriers on PbTe and $Pb_{0.8}Sn_{0.2}Te$. *Appl. Phys. Lett.* **1970**, *16*, 375−377.
(57) Baker, W. D.; Milnes, A. G. Schottky Barriers on ZnTe. *J. Appl. Phys.* **1972**, *43*, 5152−5153.
(58) Popescu, A.; Woods, L. M.; Martin, J.; Nolas, G. S. Model of Transport Properties of Thermoelectric Nanocomposite Materials. *Phys. Rev. B* **2009**, *79*, 205302−205308.
(59) Kishimoto, K.; Yamamoto, K.; Koyanagi, T. Influences of Potential Barrier Scattering on the Thermoelectric Properties of Sintered *n*-Type PbTe with a Small Grain Size. *Jpn. J. Appl. Phys.* **2003**, *42*, 501−508.
(60) Kao, K. C. *Dielectric Phenomena in Solids*; Elsevier Academic Press: London, 2004.